



UNIVERSITY OF LEEDS

This is a repository copy of *Dust Continuum Emission and the Upper Limit Fluxes of Submillimeter Water Lines of the Protoplanetary Disk around HD 163296 Observed by ALMA*.

White Rose Research Online URL for this paper:

<https://eprints.whiterose.ac.uk/145305/>

Version: Published Version

---

**Article:**

Notsu, S, Akiyama, E, Booth, A et al. (6 more authors) (2019) Dust Continuum Emission and the Upper Limit Fluxes of Submillimeter Water Lines of the Protoplanetary Disk around HD 163296 Observed by ALMA. *Astrophysical Journal*, 875 (2). 96. ISSN 0004-637X

<https://doi.org/10.3847/1538-4357/ab0ae9>

---

© 2019. The American Astronomical Society. All rights reserved. Reproduced in accordance with the publisher's self-archiving policy. <https://doi.org/10.3847/1538-4357/ab0ae9>.

**Reuse**

Items deposited in White Rose Research Online are protected by copyright, with all rights reserved unless indicated otherwise. They may be downloaded and/or printed for private study, or other acts as permitted by national copyright laws. The publisher or other rights holders may allow further reproduction and re-use of the full text version. This is indicated by the licence information on the White Rose Research Online record for the item.

**Takedown**

If you consider content in White Rose Research Online to be in breach of UK law, please notify us by emailing [eprints@whiterose.ac.uk](mailto:eprints@whiterose.ac.uk) including the URL of the record and the reason for the withdrawal request.



[eprints@whiterose.ac.uk](mailto:eprints@whiterose.ac.uk)  
<https://eprints.whiterose.ac.uk/>



# Dust Continuum Emission and the Upper Limit Fluxes of Submillimeter Water Lines of the Protoplanetary Disk around HD 163296 Observed by ALMA

Shota Notsu<sup>1,9,10</sup> , Eiji Akiyama<sup>2</sup> , Alice Booth<sup>3</sup>, Hideko Nomura<sup>4,11</sup> , Catherine Walsh<sup>3</sup> , Tomoya Hirota<sup>5</sup> ,  
Mitsuhiko Honda<sup>6,12</sup> , Takashi Tsukagoshi<sup>5</sup> , and T. J. Millar<sup>7,8</sup> 

<sup>1</sup> Department of Astronomy, Graduate School of Science, Kyoto University, Kitashirakawa-Oiwake-cho, Sakyo-ku, Kyoto, Kyoto 606-8502, Japan  
[snotsu@kusastro.kyoto-u.ac.jp](mailto:snotsu@kusastro.kyoto-u.ac.jp)

<sup>2</sup> Institute for the Advancement of Higher Education, Hokkaido University, Kita 17, Nishi 8, Kita-ku, Sapporo, Hokkaido 060-0817, Japan

<sup>3</sup> School of Physics and Astronomy, University of Leeds, Leeds, LS2 9JT, UK

<sup>4</sup> Department of Earth and Planetary Science, Tokyo Institute of Technology, 2-12-1 Ookayama, Meguro-ku, Tokyo 152-8551, Japan

<sup>5</sup> National Astronomical Observatory of Japan, 2-21-1 Osawa, Mitaka, Tokyo 181-8588, Japan

<sup>6</sup> Department of Physics, School of Medicine, Kurume University, 67 Asahi-machi, Kurume, Fukuoka 830-0011, Japan

<sup>7</sup> Astrophysics Research Centre, School of Mathematics and Physics, Queen's University Belfast, University Road, Belfast, BT7 1NN, UK

<sup>8</sup> Leiden Observatory, Leiden University, P.O. Box 9513, 2300 RA Leiden, The Netherlands

Received 2018 December 6; revised 2019 February 22; accepted 2019 February 25; published 2019 April 19

## Abstract

In this paper, we analyze the upper limit fluxes of submillimeter ortho- $\text{H}_2^{16}\text{O}$  321 GHz, para- $\text{H}_2^{18}\text{O}$  322 GHz, and HDO 335 GHz lines from the protoplanetary disk around the Herbig Ae star HD 163296, using the Atacama Large Millimeter/Submillimeter Array. These water lines are considered to be the best candidate submillimeter lines to locate the position of the  $\text{H}_2\text{O}$  snowline, on the basis of our previous model calculations. We compare the upper limit fluxes with the values calculated by our models with dust emission included, and we constrain the line-emitting region and the dust opacity from the observations. We conclude that, if the outer edge of the region with a high water abundance and the position of the water snowline are both beyond 8 au, then the millimeter dust opacity  $\kappa_{\text{mm}}$  will have a value larger than  $2.0 \text{ cm}^2 \text{ g}^{-1}$ . In addition, the position of the water snowline must lie inside 20 au if the millimeter dust opacity  $\kappa_{\text{mm}}$  is  $2.0 \text{ cm}^2 \text{ g}^{-1}$ . Future observations of the dust continuum emission at higher angular resolution and submillimeter water lines with a longer observation time are required to clarify the detailed structures and the position of the  $\text{H}_2\text{O}$  snowline in the disk midplane.

**Key words:** astrochemistry – ISM: molecules – protoplanetary disks – stars: formation – stars: individual (HD 163296) – submillimeter: planetary systems

## 1. Introduction

Recently, high angular resolution and sensitivity observations of near-infrared dust scattered light (e.g., Gemini Planet Imager on Gemini-South and SPHERE on the Very Large Telescope) and submillimeter dust continuum emission (e.g., Atacama Large Millimeter/submillimeter Array (ALMA)) have found one or multiple gaps and rings for various protoplanetary disks. The origins of these multiple gap and ring patterns are still under discussion (see also Section 4), and the disk around HD 163296 is a great example of a disk that shows planet-induced structures at multiple wavelengths. Isella et al. (2016) observed the 232 GHz (1.3 mm, Band 6) dust continuum emission of the disk around HD 163296 with a spatial resolution of around 20 au using ALMA, and revealed three dark concentric rings that indicate the presence of dust-depleted gaps at about 50, 83, and 137 au from the central star (see also Zhang et al. 2016; Andrews et al. 2018; Isella et al. 2018; Liu et al. 2018; Teague et al. 2018; Dent et al. 2019). Pinte et al. (2018) presented the detection of a large, localized deviation from Keplerian velocity in the  $^{12}\text{CO}$   $J = 2 - 1$  and

$J = 3 - 2$  emission lines of this object obtained by ALMA, and the observed velocity pattern is consistent with the dynamical effect of a two-Jupiter-mass planet orbiting at a radius  $\sim 260$  au from the star. In addition, Teague et al. (2018) found that the rotation curves of  $^{12}\text{CO}$ ,  $^{13}\text{CO}$ , and  $\text{C}^{18}\text{O}$   $J = 2 - 1$  emission lines of this object obtained by ALMA had substantial deviations caused by local perturbations in the radial pressure gradient, which they explained as due to two Jupiter-mass planets at 83 and 137 au. Several near-infrared dust scattered light observations (Monnier et al. 2017; Guidi et al. 2018) for this object also detected ringed emission around 65 au, a position consistent with the first bright dust continuum ring observed by ALMA. Here, we note that the observation in the recent ALMA Disk Substructures at High Angular Resolution Project (DSHARP) of the 1.3 mm dust continuum ( $\Delta r \sim 4$  au) of the disk around HD 163296 found new small-scale structures, such as a dark gap at 10 au, a bright ring at 15 au, a dust crescent at a radius of 55 au, and several fainter azimuthal asymmetries (Andrews et al. 2018; Isella et al. 2018).

Measuring the position of the water snowline (which corresponds to the sublimation front of water molecules, e.g., Hayashi 1981; Hayashi et al. 1985) by observations in protoplanetary disks is important because it will constrain the dust-grain evolution and planet formation (e.g., Öberg et al. 2011; Oka et al. 2011; Okuzumi et al. 2012; Ros & Johansen 2013; Banzatti et al. 2015; Piso et al. 2015, 2016; Cieza et al. 2016; Pinilla et al. 2017; Schoonenberg et al. 2017), and the origin of water on terrestrial planets (e.g., Morbidelli et al. 2000, 2012, 2016; Walsh et al. 2011; Ida & Guillot 2016;

<sup>9</sup> JSPS (Japan Society for the Promotion of Science) Overseas Research Fellow (from 2019 April).

<sup>10</sup> Leiden Observatory, Leiden University, P.O. Box 9513, 2300 RA Leiden, The Netherlands (from 2019 April).

<sup>11</sup> National Astronomical Observatory of Japan, 2-21-1 Osawa, Mitaka, Tokyo 181-8588, Japan (from 2019 April).

<sup>12</sup> Faculty of Biosphere-Geosphere Science, Okayama University of Science, 1-1 Ridai-chou, Kita-ku, Okayama, Okayama 700-0005, Japan (from 2019 April).

Sato et al. 2016; Raymond & Izidoro 2017). Water ice features in disks have been detected through low-dispersion spectroscopic observations (Malfait et al. 1999; Terada et al. 2007; Honda et al. 2009, 2016; McClure et al. 2012, 2015; Min et al. 2016; Terada & Tokunaga 2017). However, it is difficult to directly locate the H<sub>2</sub>O snowline through such water ice observations, because the spatial resolution of existing telescopes is insufficient.

H<sub>2</sub>O lines from disks have been detected through recent space infrared spectroscopic observations, such as *Spitzer*/IRS and *Herschel*/PACS, HIFI (for more details, see, e.g., Carr & Najita 2008; Pontoppidan et al. 2010a; Hogerheijde et al. 2011; Salyk et al. 2011; Fedele et al. 2012, 2013; Meeus et al. 2012; Riviere-Marichalar et al. 2012; Kamp et al. 2013; Podio et al. 2013; Zhang et al. 2013; van Dishoeck et al. 2014; Antonellini et al. 2015, 2016, 2017; Blevins et al. 2016; Banzatti et al. 2017; Du et al. 2017). However, these lines mainly trace the disk surface and the cold water reservoir outside the H<sub>2</sub>O snowline. Water line profiles were detected by ground-based near-infrared and mid-infrared spectroscopic observations using the Keck Observatory, VLT, and Gemini North/TEXES for some bright T Tauri disks<sup>13</sup> (e.g., Salyk et al. 2008, 2019; Pontoppidan et al. 2010b; Mandell et al. 2012). Those observations suggested that the hot water vapor resides in the inner part of the disks; however, the spatial and spectral resolutions were not sufficient to investigate detailed structures, such as the position of the H<sub>2</sub>O snowline. In addition, the observed lines, with large Einstein *A* coefficients, are sensitive to the water vapor in the disk surface and are potentially polluted by slow disk winds.

In our previous papers (Notsu et al. 2015, 2016, 2017, 2018), on the basis of our calculations of disk chemical structures and water line profiles, we proposed how to identify the position of the H<sub>2</sub>O snowline directly by analyzing the Keplerian profiles of water lines, which can be obtained by high-dispersion spectroscopic observations across a wide range of wavelengths (from mid-infrared to submillimeter, e.g., ALMA, SPICA). We selected candidate water lines to locate the H<sub>2</sub>O snowline based on specific criteria. We concluded that lines that have small Einstein *A* coefficients ( $A_{ul} = 10^{-6} \sim 10^{-3} \text{ s}^{-1}$ ) and relatively high upper state energies ( $E_{up} \sim 1000 \text{ K}$ ) trace the hot water reservoir within the H<sub>2</sub>O snowline, and can locate the position of the H<sub>2</sub>O snowline. In these candidate lines, the contribution of the optically thick hot midplane inside the H<sub>2</sub>O snowline is large compared with that of the outer optically thin surface layer. This is because the intensities of lines from the optically thin region are proportional to the Einstein *A* coefficient. Moreover, the contribution of the cold water reservoir outside the H<sub>2</sub>O snowline is also small, because lines with high excitation energies are not emitted from the regions at a low temperature. In addition, since the number densities of the ortho- and para-H<sub>2</sub><sup>18</sup>O molecules are about 1/560 times smaller than their <sup>16</sup>O analogs, they trace deeper into the disk than the ortho-H<sub>2</sub><sup>16</sup>O lines (down to  $z = 0$ ), and lines with relatively smaller upper state energies ( $\sim$  a few 100 K) can also locate the position of the H<sub>2</sub>O snowline. Thus, these H<sub>2</sub><sup>18</sup>O lines are potentially better probes of the position of the H<sub>2</sub>O snowline at the disk midplane, depending on the dust optical depth (Notsu et al. 2018).

The position of the H<sub>2</sub>O snowline of a Herbig Ae disk exists at a larger radius compared with that around less massive and cooler T Tauri stars. In addition, the position of H<sub>2</sub>O snowline migrates closer to the star as the disk becomes older and the mass accretion rate to the central star becomes smaller (e.g., Oka et al. 2011; Harsono et al. 2015). Therefore, it is expected to be easier to observe the candidate water lines, and thus identify the location of the H<sub>2</sub>O snowline, in Herbig Ae disks, younger T Tauri disks (e.g., HL Tau, ALMA Partnership et al. 2015; Banzatti et al. 2015; Zhang et al. 2015; Okuzumi et al. 2016), and disks around FU Orionis-type stars (e.g., V883 Ori, Cieza et al. 2016; van't Hoff et al. 2018).

In this paper, we report our ALMA observations of submillimeter water lines (ortho-H<sub>2</sub><sup>16</sup>O 321 GHz, para-H<sub>2</sub><sup>18</sup>O 322 GHz, and HDO 335 GHz) from the protoplanetary disk around the Herbig Ae star HD 163296. These lines are considered to be the prime candidate water lines available at submillimeter wavelengths to locate the position of the H<sub>2</sub>O snowline (Notsu et al. 2015, 2016, 2017, 2018). We also report the dust continuum emission from the disk around HD 163296 at a spatial resolution of around 15 au, that confirms the multi-ringed and gapped structure originally found in previous observations (e.g., Isella et al. 2016; Dent et al. 2019). Section 2 outlines the observational setup and our data reduction process, and introduces the previous work on our target. The results and a discussion of the water line observations are described in Section 3, and dust continuum emission is reported in Section 4. In Section 5, we provide our conclusions.

## 2. Observations

### 2.1. Observational Setup and Data Reduction

The high-spatial-resolution continuum and water line observations at Band 7 ( $\lambda \sim 0.9 \text{ mm}$ ) with ALMA were carried out in Cycle 3 on 2016 September 16 (2015.1.01259.S, PI: S. Notsu). In the observation period, 40 of the 12 m antennas were operational and the maximum baseline length was 2483.5 m. The correlator was configured to detect dual polarizations in four spectral windows with a bandwidth of 1.875 GHz and a resolution of 1953.125 kHz each, resulting in a total bandwidth of 7.5 GHz. The spectral windows were centered at 320.844 GHz (SPW1), 322.740 GHz (SPW2), 332.844 GHz (SPW3), and 334.740 GHz (SPW4), covering ortho-H<sub>2</sub><sup>16</sup>O 321 GHz, para-H<sub>2</sub><sup>18</sup>O 322 GHz, and HDO 335 GHz lines (see also Table 1). The first local oscillator frequency was tuned at 327.72597 GHz in order to avoid a strong atmospheric absorption around 325 GHz. The integration time on source (HD 163296) is 0.723 hr (43.35 minutes). This integration time is around 20% of our requested time in our Cycle 3 proposal for the clear detection of water lines.

The phase was calibrated by observations of J1742-1517 and J1751-1950 approximately every 10 minutes, and J1733-1304 was used for absolute flux calibration. The observed passbands were calibrated by J1924-2914. The visibility data were reduced and calibrated using the Common Astronomical Software Application package, version 4.7.2. The corrected visibilities were imaged using the CLEAN algorithm with Briggs weighting with a robust parameter of 0.5 after calibration of the bandpass, gain in amplitude and phase, and absolute flux scaling, and then flagging for aberrant data. The *uv* sampling of our Band 7 data is relatively sparse. Since in

<sup>13</sup> In the remainder of this paper, we define the protoplanetary disks around T Tauri/Herbig Ae stars as “T Tauri/Herbig Ae disks.”

**Table 1**  
Parameters and Observed Upper Limits of Our Target Water Lines in ALMA Band 7

Isotope	$J_{K_a K_c}$	$\lambda$ ( $\mu\text{m}$ )	Frequency (GHz)	$A_{ul}$ ( $\text{s}^{-1}$ )	$E_{up}$ (K)	$3\sigma$ Peak Flux Density <sup>a</sup> (mJy)	$3\sigma$ Total Flux <sup>a,b</sup> ( $\text{W m}^{-2}$ )
ortho- $\text{H}_2^{16}\text{O}$	10 <sub>20</sub> -9 <sub>36</sub>	933.2767	321.22568	$6.17 \times 10^{-6}$	1861.2	<8.7	$<5.3 \times 10^{-21}$
para- $\text{H}_2^{18}\text{O}$	5 <sub>15</sub> -4 <sub>22</sub>	929.6894	322.46517	$1.06 \times 10^{-5}$	467.9	<13.9	$<8.5 \times 10^{-21}$
HDO	3 <sub>31</sub> -4 <sub>22</sub>	893.8476	335.39550	$2.61 \times 10^{-5}$	335.3	<7.3	$<6.3 \times 10^{-21}$

**Notes.**

<sup>a</sup> In calculating the upper limit values of peak flux densities and total fluxes, we integrate the line flux components within 20 au (circular aperture) from the central star. In addition, the  $\sigma$  value is the root-mean-square value of peak flux density.

<sup>b</sup> In calculating the upper limit values of total fluxes, we set the velocity width of the double-peaked profiles as  $30 \text{ km s}^{-1}$ , according to the velocity width of model-calculated line profiles (see Figures 2 and 3).

this observation we focused on the water emission lines from the hot region inside the  $\text{H}_2\text{O}$  snowline ( $\lesssim 14$  au), we do not have good  $uv$  coverage at shorter baselines. From previous observations, it is known that the dust emission extends to  $>100$  au. Thus, in order to recover the missing flux, especially in the outer disk, we have combined Band 7 archival ACA (Atacama Compact Array) data (2016.1.00884.S, PI: V. Guzman) with our Band 7 data in our dust continuum imaging after applying a phase shift to account for proper motion and different input phase centers. In addition to the usual CLEAN imaging, we performed self-calibration of the continuum emission to improve the sensitivity and image quality. The obtained solution table of the self-calibration for the continuum emission was applied to the visibilities of the lines. The spatial resolution of the final image is  $0.174 \times 0.124$  arcsec, with a position angle (PA) of  $76.799$  deg for Band 7, corresponding to  $17.7 \text{ au} \times 12.6 \text{ au}$ . The noise level (rms) of the Band 7 image is around  $0.1 \text{ mJy beam}^{-1}$ .

We also used ALMA Band 6 calibrated archival data (2013.1.00601.S, PI: A. Isella) of this object, which was obtained in ALMA Cycle 2, to compare the dust continuum images between Bands 6 and 7. We generate the Band 6 image with Briggs weighting at a robust parameter of 0.5. The spatial resolution of the final image is  $0.278 \times 0.184$  arcsec, with a PA of  $-87.987$  deg for Band 6, corresponding to  $28.2 \text{ au} \times 18.7 \text{ au}$ . The spatial resolution of this calibrated archival data is  $\sim 1.7$  times larger than that reported in Isella et al. (2016) ( $0.22 \times 0.14$  arcsec, corresponding to  $22.3 \text{ au} \times 14.2 \text{ au}$ ), in which they generated the self-calibrated continuum image with a different Briggs weighting parameter,  $-1$  (uniform weighting). The noise level (rms) of the calibrated archival data of the Band 6 image is around  $0.5 \text{ mJy beam}^{-1}$ .

The total disk fluxes are  $1.85 \text{ Jy}$  in Band 7, and  $0.68 \text{ Jy}$  in Band 6, giving a spectral index  $\alpha_{\text{mm}}$  of  $\sim 2.7$ . This is in reasonable agreement with that measured by Pinilla et al. (2014) ( $2.73 \pm 0.44$ ) and Guidi et al. (2016), and a bit larger than that measured by Dent et al. (2019) ( $2.1 \pm 0.3$ ).

## 2.2. Target

Our target HD 163296 is an isolated, young ( $\sim 5$  Myr), and intermediate-mass ( $\sim 2.3 M_{\odot}$ ) Herbig Ae star and has no evidence of a stellar binary companion. It is relatively nearby, and it is surrounded by a well-studied gas-rich disk with no hint of an inner hole (group II, e.g., Honda et al. 2015). Here, we note that according to the recent *Gaia* data release 2,<sup>14</sup> the distance obtained by *Hipparcos* measurement in the past

( $d \sim 122$  pc, e.g., Perryman et al. 1997; van den Ancker et al. 1997) was corrected to  $d \sim 101.5$  pc (Gaia Collaboration et al. 2018). In this paper, we adopt this new distance value (101.5 pc). It has a relatively large inclination angle ( $i \sim 42$  deg, Isella et al. 2016), and thus we expected the characteristic double-peaked velocity profiles of gas in Keplerian rotation with large velocity widths ( $\sim 30 \text{ km s}^{-1}$ ) due to the compact emitting area, which was suitable to detect the position of the  $\text{H}_2\text{O}$  snowline. In addition, this object has been observed in many transitions at various wavelengths. The spectrally resolved CO lines in the submillimeter show the characteristic double-peaked profiles of gas in Keplerian rotation (e.g., Dent et al. 2005; Akiyama et al. 2011).

The CO snowline of this object is resolved directly using  $\text{C}^{18}\text{O}$ ,  $\text{N}_2\text{H}^+$ , and  $\text{DCO}^+$  line data obtained by ALMA (e.g., Qi et al. 2011, 2015; Mathews et al. 2013; Salinas et al. 2017, 2018). Previous ALMA observations showed that the continuum emission has a local maximum near the location of the CO snowline (Guidi et al. 2016; Zhang et al. 2016). The CO snowline position is around 75 au, using the new *Gaia* data. In addition, the measurements of the spectral index  $\alpha$  indicated the presence of large grains and pebbles ( $\sim 1$  cm) in the inner regions of the disk (inside 40 au) and smaller grains, consistent with ISM sizes, in the outer disk (beyond 125 au), which would suggest a grain size distribution consistent with an enhanced production of large grains at the CO snowline and consequent transport to the inner regions (Guidi et al. 2016). Boneberg et al. (2016) suggested that by combining their  $\text{C}^{18}\text{O}$  line models, previous CO snowline observations, and spectral energy distributions, the gas-to-dust-mass ratio  $g/d$  would be low ( $<20$ ) within the CO snowline, the disk gas mass is  $\sim (8-30) \times 10^{-3} M_{\odot}$ , and the millimeter dust opacity  $\kappa_{\text{mm}}$  is  $\sim 3 \text{ cm}^2 \text{ g}^{-1}$ , assuming the values of  $\text{C}^{18}\text{O}$  abundances reported in star-forming clouds ( $\sim 10^{-7}-10^{-6}$ ). They also suggested that the value of  $g/d$  would be larger (up to ISM-like value,  $\sim 100$ ) if they assume lower  $\text{C}^{18}\text{O}$  abundance because of CO depletion.

According to Reboussin et al. (2015) and Bosman et al. (2018), the C atoms generated through CO photodissociation in the upper layers can be effectively removed through formation of species other than CO (e.g.,  $\text{CO}_2$  and  $\text{CH}_4$ ). Photodissociation is normally localized in the disk surface, and the  $\text{C}^{18}\text{O}$  abundance may be affected only if the CO dissociating photons penetrate to the disk midplane, or if the surface continued to be depleted of CO over very long timescales. In addition, significant depletion of CO will occur in the outer cold parts of the disks with a high cosmic-ray rate (Bosman et al. 2018; Schwarz et al. 2018). Here, we note that in one relatively old T

<sup>14</sup> <https://www.cosmos.esa.int/web/gaia/dr2>

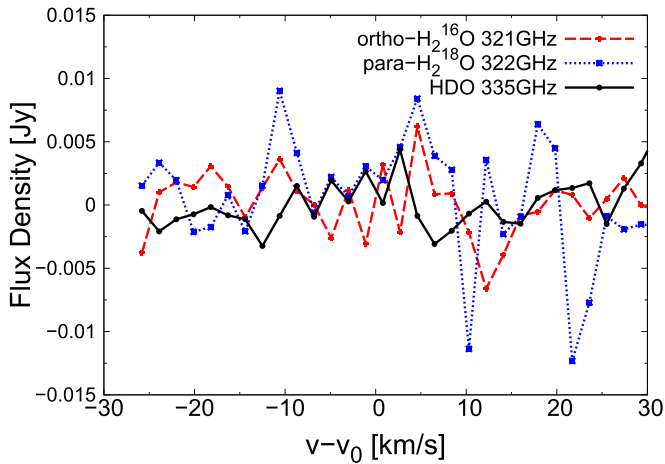


**Figure 1.** Observed flux densities around the line centers of the ortho- $\text{H}_2^{16}\text{O}$  line at 321 GHz (red dashed line with cross symbols), the para- $\text{H}_2^{18}\text{O}$  line (blue dotted line with filled square symbols) at 322 GHz, and the HDO line at 335 GHz (black solid line with circle symbols) of the disk around HD 163296, with a velocity resolution  $\Delta v = 1.9 \text{ km s}^{-1}$ . In obtaining the observed line flux densities, we adopted a circular aperture with radius 20 au.

Tauri disk around TW Hya, the abundances of CO and its isotopologues are observed as about 100 times lower than their ISM values (Favre et al. 2013; Nomura et al. 2016; Schwarz et al. 2016; Zhang et al. 2017).

Carney et al. (2019) derived the  $3\sigma$  disk-integrated intensity upper limits of methanol ( $\text{CH}_3\text{OH}$ ) emission lines in ALMA Bands 6 and 7 toward the disk around HD 163296, and found that the disk is less abundant in methanol with respect to formaldehyde ( $\text{H}_2\text{CO}$ ) compared to the disk around TW Hya. They discussed possible reasons for the lower  $\text{CH}_3\text{OH}/\text{H}_2\text{CO}$  ratio, such as differences in the disk structure and/or  $\text{CH}_3\text{OH}$  and  $\text{H}_2\text{CO}$  desorption processes, uncertainties in the grain surface formation efficiency, and a higher rate of gas-phase formation of  $\text{H}_2\text{CO}$ . They estimated additional observation times required for ALMA detections of  $\text{CH}_3\text{OH}$  lines in the disk around HD 163296, depending on the different  $\text{CH}_3\text{OH}/\text{H}_2\text{CO}$  ratios.

The position of the  $\text{H}_2\text{O}$  snowline of a disk around a Herbig Ae star with a stellar luminosity of  $36 L_\odot$  is  $\sim 14$  au from the central star, on the basis of our calculations (Notsu et al. 2017, 2018). Previous infrared observations of HD 163296 detected far-infrared water lines. Meeus et al. (2012) and Fedele et al. (2012, 2013) reported that three far-infrared ortho- $\text{H}_2^{16}\text{O}$  emission lines (63.32, 71.95, 78.74  $\mu\text{m}$ ) are detected at slightly above  $3\sigma$  with *Herschel*/PACS. These lines have large Einstein  $A$  coefficients ( $A_{\text{ul}} \sim 1 \text{ s}^{-1}$ ) and the spectral resolving power of the data was not high ( $R \sim \lambda/\Delta\lambda \sim 1000\text{--}3000$ ). They argued that these  $\text{H}_2\text{O}$  lines are emitted from an upper hot water layer at radial distances  $\sim 20$  au, where water formation is driven by high-temperature neutral–neutral reactions. This argument is consistent with the results of our model calculations of lines with large Einstein  $A$  coefficients (Notsu et al. 2016, 2017, 2018).

### 3. Water Line Emission

#### 3.1. Upper Limit of the Water Line Fluxes

Figure 1 shows the observed flux densities around the line centers of the ortho- $\text{H}_2^{16}\text{O}$  line at 321 GHz, the para- $\text{H}_2^{18}\text{O}$  line at 322 GHz, and the HDO line at 335 GHz of the disk inside

20 au around HD 163296, with a velocity resolution  $\Delta v = 1.9 \text{ km s}^{-1}$ . The detailed parameters, such as transition quantum numbers ( $J_{K_a, K_c}$ ), wavelength  $\lambda$ , frequency,  $A_{\text{ul}}$ ,  $E_{\text{up}}$ ,  $3\sigma^{15}$  peak flux densities, and  $3\sigma$  total fluxes of lines are listed in Table 1. These lines have not been detected, and we conduct our subsequent analyses using the extracted upper limits for the line fluxes. In calculating the upper limits, we assume that the velocity width of the double-peaked profiles is  $30 \text{ km s}^{-1}$ , on the basis of the velocity width of model-calculated line profiles (see Figures 2 and 3). Depending on the shapes of model line profiles, the actual velocity widths between the line peaks could be smaller than  $30 \text{ km s}^{-1}$ , especially in the cases with large snowline positions. Therefore, in these cases the upper limit values of line fluxes would be overestimated (see Figures 2 and 3 and Table 1).

In Figures 2 and 3, we compare the upper limit fluxes with the values from our model water line calculations with dust emission (Notsu et al. 2015, 2016, 2017, 2018), to constrain the dust opacity and the line-emitting region, respectively, and to estimate the necessary observation time for a future clear detection. We calculate the model line profiles with different dust opacity values and different outer edges of the region with a high water vapor abundance. When we calculate these model line profiles, we include both dust and gas emission components, and we subtract the dust continuum emission component (the values of the calculated fluxes at  $v - v_0 = \pm\infty$ ) to show the line emission component more clearly.

In our models, we first adopted the physical model of a steady, axisymmetric Keplerian accretion disk with a viscous parameter  $\alpha = 10^{-2}$ , a mass accretion rate  $\dot{M} = 10^{-8} M_\odot \text{ yr}^{-1}$ , and a gas-to-dust-mass ratio  $g/d = 100$  surrounding a Herbig Ae star with stellar mass  $M_* = 2.5 M_\odot$ , stellar radius  $R_* = 2.0 R_\odot$ , and effective temperature  $T_* = 10,000 \text{ K}$  (Nomura & Millar 2005; Nomura et al. 2007; Walsh et al. 2015). The top panels of Figure 4 show the total gas number density in  $\text{cm}^{-3}$  (top left panel) and the gas temperature in K (top right panel) of a disk around a Herbig Ae star (see also Figure 1 of Notsu et al. 2017). Next, we calculated the water gas and ice distributions in the disk using chemical kinetics. The large chemical network (Woodall et al. 2007; Walsh et al. 2010, 2012, 2015) we use to calculate the disk molecular abundances includes gas-phase reactions and gas-grain interactions (freeze-out, and thermal and nonthermal desorption). The bottom panel of Figure 4 shows the fractional abundance (relative to total hydrogen nuclei density) distribution of water gas of the disk (see also Section 3.1 and Figure 2 of Notsu et al. 2017). We found that the water abundance is high (up to  $10^{-4}$ ) in the inner region, with higher temperature ( $\sim 170 \text{ K}$ ) within  $\sim 7\text{--}8$  au, and relatively high ( $10^{-8}$ ) between  $7\text{--}8$  and  $14$  au (at the position of the  $\text{H}_2\text{O}$  snowline,  $\sim 120 \text{ K}$ ) near the equatorial plane. In addition, it is relatively high ( $\sim 10^{-8}\text{--}10^{-7}$ ) in the hot surface layer and the photodesorbed region of the outer disk, compared to its value ( $10^{-12}$ ) in the regions outside the  $\text{H}_2\text{O}$  snowline near the equatorial plane. Using these data, we calculated the profiles of water emission lines. For more details, see Notsu et al. (2015, 2016, 2017, 2018).

For the calculation of line profiles, we modified the 1D code RATRAN<sup>16</sup> (Hogerheijde & van der Tak 2000). The data for the line parameters are adopted from the Leiden Atomic and

<sup>15</sup> The  $\sigma$  value is the rms value of peak flux density.

<sup>16</sup> <http://home.strw.leidenuniv.nl/~michiela/ratran/>

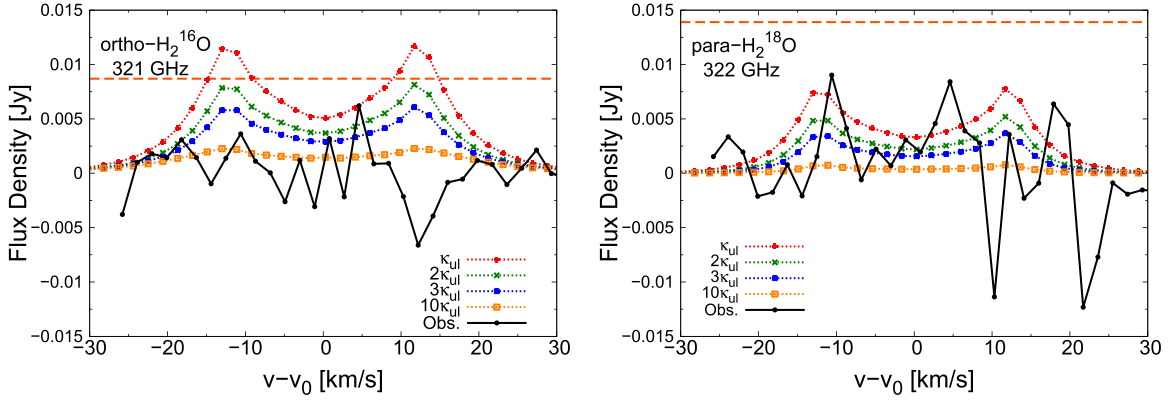


**Figure 2.** Profiles of the ortho- $\text{H}_2^{16}\text{O}$  line at 321 GHz (left panel) and the para- $\text{H}_2^{18}\text{O}$  line (right panel) at 322 GHz inside 20 au, with a velocity resolution  $d\nu = 1.9 \text{ km s}^{-1}$ . The black solid line with circle symbols is the observed flux density of the disk around HD 163296. Other lines are the results of our Herbig Ae disk model calculations (see also Notsu et al. 2017, 2018). The red dotted lines with cross symbols are the line profiles of our original Herbig Ae disk model. In the line profiles with green dotted lines with cross symbols, blue dotted lines with filled square symbols, and orange dotted lines with square symbols, we set the values of dust opacity  $\kappa_{\text{ul}}$  2, 3, and 10 times larger than our original value. The horizontal red dashed lines show the values of observed  $3\sigma$  peak flux densities around line centers (see also Table 1).

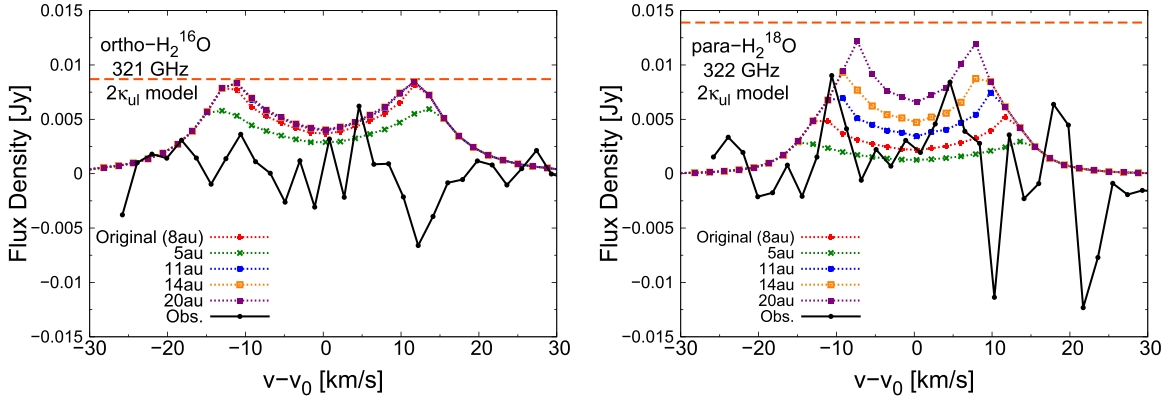


**Figure 3.** Profiles of the ortho- $\text{H}_2^{16}\text{O}$  line at 321 GHz (left panel) and the para- $\text{H}_2^{18}\text{O}$  line (right panel) at 322 GHz inside 20 au, with a velocity resolution  $d\nu = 1.9 \text{ km s}^{-1}$ . The black solid line with circle symbols is the observed flux density of the disk around HD 163296. Other lines are the line profiles that are obtained by our Herbig Ae disk model calculations (see also Notsu et al. 2017, 2018). The red dotted lines with cross symbols are the line profile with our original water vapor abundance distributions. In other line profiles, we artificially change the outer edge of the region with a high  $\text{H}_2\text{O}$  water vapor abundance ( $\sim 10^{-5}$ – $10^{-4}$ ) region to 5 au (green dotted lines with cross symbols), 11 au (blue dotted lines with filled square symbols), 14 au (orange dotted lines with perforated square symbols), and 20 au (purple dotted lines with square symbols). We set the values of dust opacity two times larger than our original value (see also Figure 2). The horizontal red dashed lines show the values of observed  $3\sigma$  peak flux densities around line centers (see also Table 1).

Molecular Database LAMDA<sup>17</sup> (Schöier et al. 2005) for the  $\text{H}_2^{16}\text{O}$  lines and from the HITRAN Database<sup>18</sup> (e.g., Rothman et al. 2013) for the  $\text{H}_2^{18}\text{O}$  lines. Here, we note that  $\text{HDO}/\text{H}_2\text{O}$  ratio is considered to be sensitive to the temperature in the disk (van Dishoeck et al. 2014). However, deuterium chemistry is not included in our chemical network, thus we only calculated the  $\text{H}_2^{16}\text{O}$  and  $\text{H}_2^{18}\text{O}$  line profiles. We set the ortho-to-para ratio of water to its high-temperature value of 3 throughout the disk (Mumma et al. 1987; Hama & Watanabe 2013; Hama et al. 2016, 2018). We set the isotope ratio of oxygen  $^{16}\text{O}/^{18}\text{O}$  to 560 throughout the disk, as Jørgensen & van Dishoeck (2010) and Persson et al. (2012) adopted. This  $^{16}\text{O}/^{18}\text{O}$  value is determined from the observations of the local interstellar medium (Wilson & Rood 1994). We do not include emission from jet components and disk winds in calculating the line profiles.

First, we fix the location of the abundant water vapor region inside the  $\text{H}_2\text{O}$  snowline and change the dust opacity. The original position of the outer edge of the water vapor abundant

region is 8 au, and that of the water snowline is 14 au. In Figure 2, we plot the model profiles of the ortho- $\text{H}_2^{16}\text{O}$  321 GHz line and the para- $\text{H}_2^{18}\text{O}$  322 GHz line with four dust opacity values. The red dotted lines with cross symbols are the line profile of our original Herbig Ae model (Notsu et al. 2017, 2018). In this model, the value of millimeter dust opacity  $\kappa_{\text{mm}}$  is  $1.0 \text{ cm}^2 \text{ g}^{-1}$ . In the line profiles with green dotted lines with cross symbols, blue dotted lines with filled square symbols, and orange dotted lines with perforated square symbols, we set the values of dust opacity 2, 3, and 10 times larger, respectively, than our original value in order to investigate the influence of dust opacity on line properties. The calculated line fluxes are listed in Table 2. We note that the dust opacity at submillimeter wavelengths can vary by a factor of around 10, depending on the properties of the dust grains (e.g., Miyake & Nakagawa 1993; Draine 2006). In our fiducial disk model, dust opacities appropriate for a dark cloud model are used and are relatively small at submillimeter wavelengths, compared to models with grain growth (see, e.g., Nomura & Millar 2005; Aikawa & Nomura 2006, and Paper I). In our model calculations, the emission of our observed Band 7 water

<sup>17</sup> <http://home.strw.leidenuniv.nl/~moldata/>

<sup>18</sup> <http://www.hitran.org>

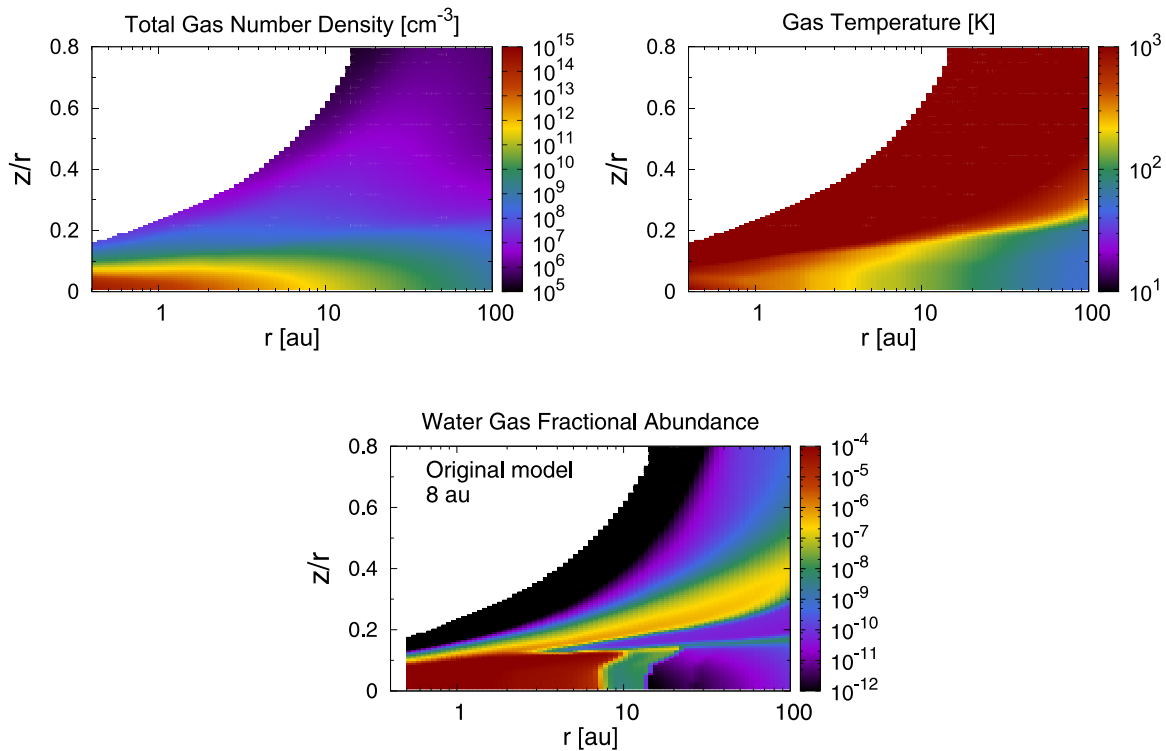


**Figure 4.** Total gas number density in  $\text{cm}^{-3}$  (top left panel), the gas temperature in K (top right panel), and fractional abundance (relative to total hydrogen nuclei density) distribution of water gas (bottom panel) of a disk around a Herbig Ae star as a function of the disk radius in au and height (scaled by the radius,  $z/r$ ) up to a maximum radius of  $r = 100$  au.

**Table 2**  
Calculated Peak Flux Densities and Total Fluxes of Our Target Water Lines in ALMA Band 7 with Different Values of Dust Opacity

Isotope	Frequency (GHz)	Peak Flux Density (mJy) <sup>a,b</sup>				Total Flux ( $\text{W m}^{-2}$ ) <sup>a,b</sup>			
		$\kappa_{\text{ori}}$	$2\kappa_{\text{ori}}$	$3\kappa_{\text{ori}}$	$10\kappa_{\text{ori}}$	$\kappa_{\text{ori}}$	$2\kappa_{\text{ori}}$	$3\kappa_{\text{ori}}$	$10\kappa_{\text{ori}}$
ortho- $\text{H}_2^{16}\text{O}$	321.22568	12.6	8.9	6.6	2.5	$2.4 \times 10^{-21}$	$2.4 \times 10^{-21}$	$1.3 \times 10^{-21}$	$6.4 \times 10^{-22}$
para- $\text{H}_2^{18}\text{O}$	322.46517	8.5	5.7	4.1	0.87	$1.9 \times 10^{-21}$	$1.8 \times 10^{-21}$	$8.4 \times 10^{-22}$	$1.9 \times 10^{-22}$

#### Notes.

<sup>a</sup> When we calculate these model line fluxes, we include both dust and gas emission components, and we subtract dust emission components after the calculation. We investigate four values of dust opacity  $\kappa$  (original value, 2, 3, and 10 times larger values) in order to investigate the influence of dust opacity on line properties.

<sup>b</sup> In calculating these model line fluxes, we integrate the flux components within 20 au (circular aperture) from the central star.

lines is optically thick in the disk midplane within the  $\text{H}_2\text{O}$  snowline. In contrast, the submillimeter dust emission is marginally optically thick. The dust emission becomes stronger as the value of the dust opacity becomes larger, and the line emission becomes obscured by the dust emission. As a result, the apparent line intensities obtained by subtracting dust continuum emission become smaller (for more details, see Notsu et al. 2017, 2018).

Here, we note that the dust properties are important because they affect the physical and chemical structure of protoplanetary disks (for details, see, e.g., Nomura et al. 2007). The total surface area of dust grains has an influence on the abundances of molecules through determining the gas and ice balance. In addition, because dust grains are the dominant opacity source in the disks, they determine the temperature profiles and the UV radiation field throughout the disk. As the location of the  $\text{H}_2\text{O}$  snowline is sensitive to the temperature, it strongly depends on the dust opacity, especially at mid-infrared wavelengths because the peak wavelength of the blackbody radiation from the disk midplane around the  $\text{H}_2\text{O}$  snowline

( $\sim 100$ – $200$  K) is mainly around  $10$ – $30 \mu\text{m}$ . The submillimeter dust opacity, on the other hand, is not a direct indicator of the dust properties that affect the location of the  $\text{H}_2\text{O}$  snowline.

According to Figure 2 and Tables 1 and 2, the observed  $3\sigma$  upper limit peak flux density of the para- $\text{H}_2^{18}\text{O}$  322 GHz line is larger than the model-calculated value with original dust opacity, and that of the ortho- $\text{H}_2^{16}\text{O}$  321 GHz line is close to the calculated value for the model with two times larger dust opacity. Here, we note that in the cases of our target water lines, most of the line emission comes from the region with a high water gas abundance ( $\gtrsim 10^{-5}$ ) in the Herbig Ae disk (Notsu et al. 2017, 2018). Therefore, we suggest that the millimeter dust opacity  $\kappa_{\text{mm}}$  is larger than  $2.0 \text{ cm}^2 \text{ g}^{-1}$  to explain the water line upper limit, if the outer edge of the water vapor abundant region and also the position of the water snowline is located at or beyond 8 au (see also Figure 3). Previous dust continuum observations of this object (e.g., Boneberg et al. 2016) show that  $\kappa_{\text{mm}} \sim 3.0 \text{ cm}^2 \text{ g}^{-1}$ . In the cases with three times larger dust opacity, the model peak flux densities correspond to around  $2\sigma$  for the ortho- $\text{H}_2^{16}\text{O}$  321 GHz

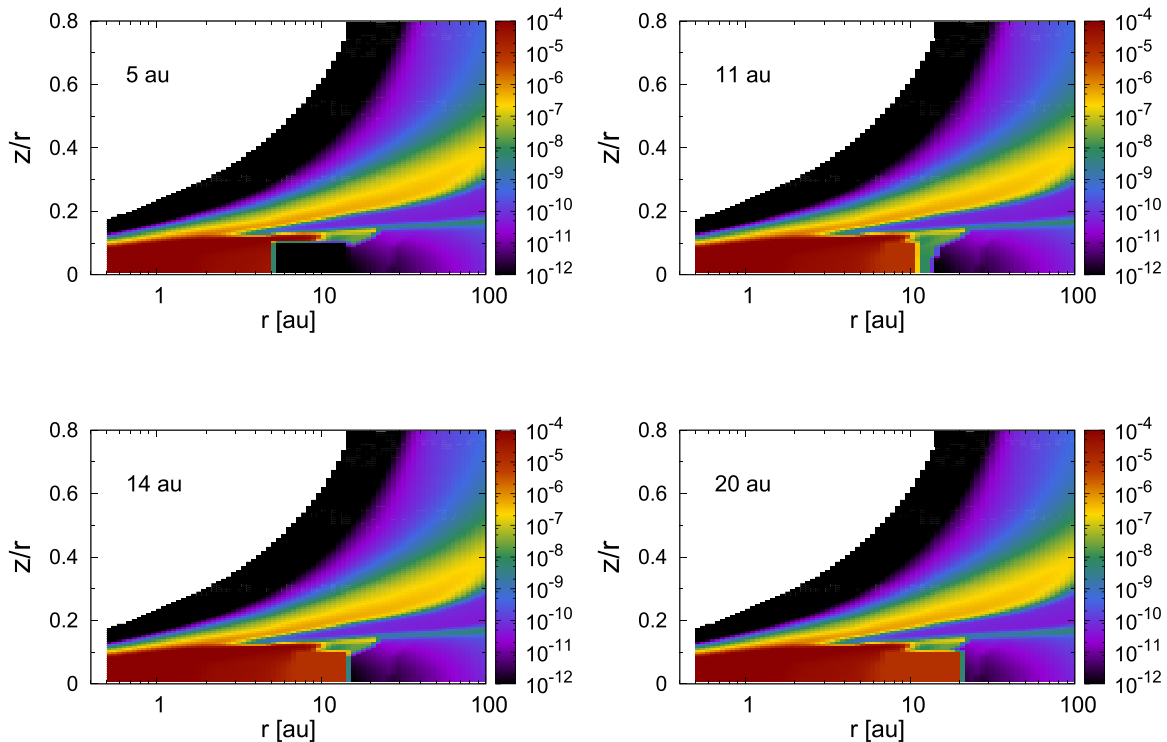


**Figure 5.** Fractional abundance (relative to total hydrogen nuclei density) distributions of water gas of a disk around a Herbig Ae star as a function of the disk radius in au and height (scaled by the radius,  $z/r$ ) up to a maximum radius of  $r = 100$  au. In these plots, we fix the dust opacity and artificially change the outer edge of the region with a high  $\text{H}_2\text{O}$  vapor abundance ( $10^{-5}$ ) from 8 au (Notsu et al. 2017, 2018; see also Figure 4 of this paper), to 5 au ( $T_g \sim 180$  K, top left panel), 11 au ( $T_g \sim 135$  K, top right panel), 14 au ( $T_g \sim 120$  K, bottom left panel), and 20 au ( $T_g \sim 100$  K, bottom right panel).

line and around  $1\sigma$  for para- $\text{H}_2^{18}\text{O}$  322 GHz line. Therefore, the observation time executed (20% of our proposed time in our Cycle 3 proposal) was not enough to test our model. Here, we note that the dust optical depth  $\tau_d$  is  $\sim 0.2$  at  $r \sim 5$  au for the model with the original dust opacity ( $\kappa_{\text{mm}} = 1.0 \text{ cm}^2 \text{ g}^{-1}$ ). Meanwhile, previous ALMA and VLA observations with lower spatial resolution suggest  $\tau_d \sim 0.55$  at  $r < 50$  au (Guidi et al. 2016), which is a few times larger than our original value at  $r \sim 5$  au.

In Figure 3, we fix the dust opacity and artificially change the outer edge of the region with a high  $\text{H}_2\text{O}$  vapor abundance ( $10^{-5}$ ) from 8 au (Notsu et al. 2017, 2018; see also Figure 4 of this paper), to 5 au ( $T_g \sim 180$  K), 11 au ( $T_g \sim 135$  K), 14 au ( $T_g \sim 120$  K, the predicted water snowline position), and 20 au ( $T_g \sim 100$  K). Figure 5 shows the artificially changed fractional abundance distributions of water vapor. We set the values of dust opacity two times larger than that of our original Herbig Ae model ( $\kappa_{\text{mm}} = 2.0 \text{ cm}^2 \text{ g}^{-1}$ ; see also Table 2 and Figure 2). The calculated line fluxes are listed in Table 3. As the region with a high water gas abundance becomes larger, the flux density of the line peaks becomes larger, and the width between the two line peaks becomes narrower. This is because the Keplerian velocity in the outer disk is smaller than that in the inner disk. Since the  $E_{\text{up}}$  of the para- $\text{H}_2^{18}\text{O}$  322 GHz line (467.9 K) is smaller than that of the ortho- $\text{H}_2^{16}\text{O}$  321 GHz line (1861.2 K), the former line profile is expected to be more sensitive to the change of position of the  $\text{H}_2\text{O}$  snowline. This is because the temperature around the  $\text{H}_2\text{O}$  snowline is around 100–200 K, and thus the line-emitting region of the former line extends around the  $\text{H}_2\text{O}$  snowline, in contrast to that of the latter line that is localized more inward (for more details, see

Notsu et al. 2017, 2018). According to the right panel of Figure 3, the position of the water snowline will be inside 20 au, if the millimeter dust opacity  $\kappa_{\text{mm}}$  is  $2.0 \text{ cm}^2 \text{ g}^{-1}$  (see also Figure 2). If  $\kappa_{\text{mm}}$  is larger than  $2.0 \text{ cm}^2 \text{ g}^{-1}$ , the outer edge of the region with a high  $\text{H}_2\text{O}$  vapor abundance, the position of the  $\text{H}_2\text{O}$  snowline can be larger than 20 au.

As we explained in Section 2.1, the integration time on source is 0.723 hr, which is around 20% of the requested time in our Cycle 3 proposal. Future observations of submillimeter water lines with a longer observation time are required to confine the water line fluxes and the position of the  $\text{H}_2\text{O}$  snowline in the disk midplane in detail for the disk around HD 163296. Following the approach undertaken by Carney et al. (2019) in their discussion of  $\text{CH}_3\text{OH}$ , we estimate the additional observation times required for the detections of water lines in the disk around HD 163296 with ALMA. The values of peak flux densities from our model calculations suggest that to obtain significant detection ( $5\sigma$ ) of the ortho- $\text{H}_2^{16}\text{O}$  321 GHz line, an integration time around 3 times longer would be needed if  $\kappa_{\text{mm}}$  is  $2.0 \text{ cm}^2 \text{ g}^{-1}$  and one around 5 times longer (similar to the requested time in our Cycle 3 proposal) would be needed if  $\kappa_{\text{mm}}$  is  $3.0 \text{ cm}^2 \text{ g}^{-1}$ , where we assume the outer edge of the region with a high  $\text{H}_2\text{O}$  vapor abundance ( $10^{-5}$ ) is larger than 8 au. Moreover, to obtain  $3\sigma$  and  $5\sigma$  detections of the para- $\text{H}_2^{18}\text{O}$  322 GHz line, around 6 and 16 times longer integration times would be needed, respectively, if  $\kappa_{\text{mm}}$  is  $2.0 \text{ cm}^2 \text{ g}^{-1}$  and the outer edge of the region with a high  $\text{H}_2\text{O}$  vapor abundance ( $10^{-5}$ ) is at 8 au. In these time estimations, we assume the same observational conditions, such as weather and numbers of antenna, as our previous observations.

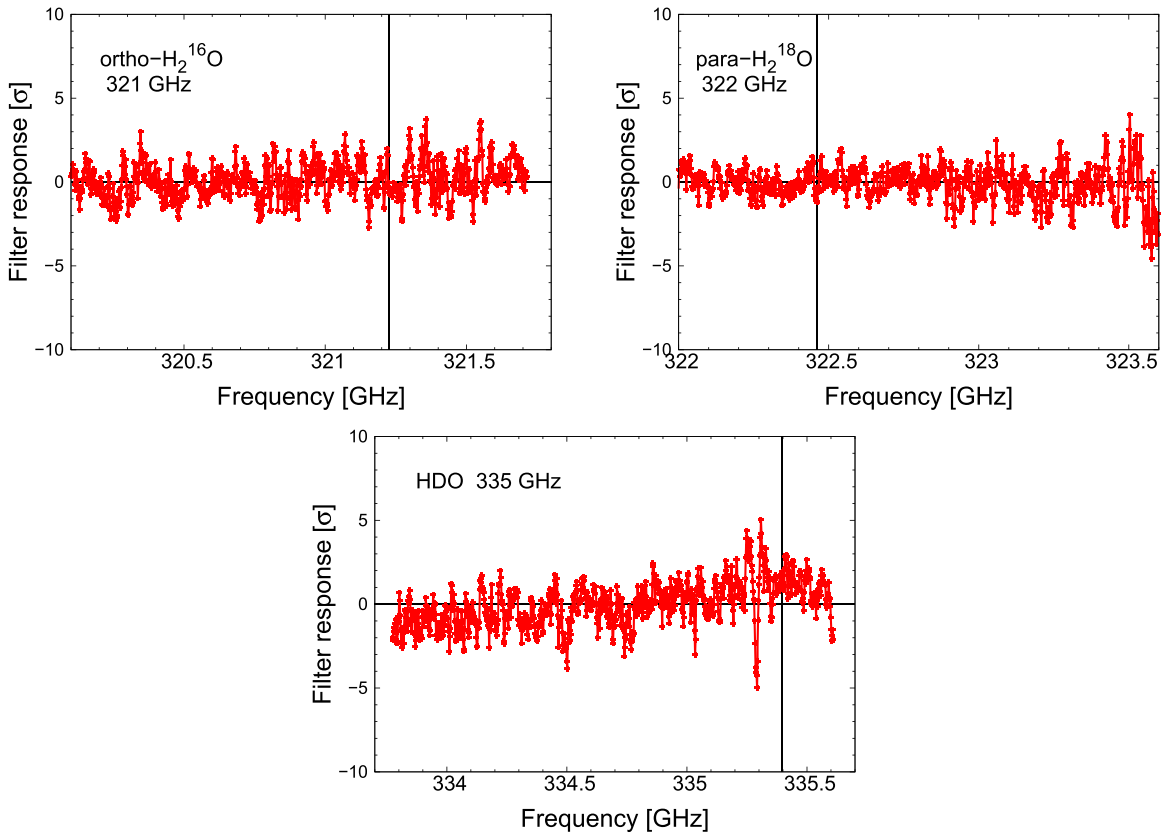


**Figure 6.** Matched filter response functions of the ortho- $\text{H}_2^{16}\text{O}$  line at 321 GHz (top left panel), the para- $\text{H}_2^{18}\text{O}$  line (top right panel) at 322 GHz, and HDO 335 GHz (bottom panel). The filter response is normalized by its standard deviation,  $\sigma$  (see also Loomis et al. 2018).

Here, we note that Carr et al. (2018) reported tentative detection ( $2\sigma$ – $3\sigma$ ) of these two water lines with ALMA toward the disk around a T Tauri star, AS 205N, which has a high-mass accretion rate ( $\dot{M} = 3 \times 10^{-7} M_{\odot} \text{yr}^{-1}$ ). The  $3\sigma$  flux density at 321 GHz of their observation is around 3 mJy.

### 3.2. Matched Filtering Analysis

Loomis et al. (2018) recently proposed a new method to detect the weak line emission from Keplerian rotating disks using observed visibility data (matched filter analysis). In this method, first we generated a Keplerian filter in the image plane with the same position and inclination angles of the source disk. The matched filter tool *VISIBLE*<sup>19</sup> then cross-correlates the transformation of this filter in the  $uv$  plane with the visibility data points from our observation (see also Carney et al. 2017, 2018, 2019; Booth et al. 2018).

Figure 6 shows the matched filter response functions of the ortho- $\text{H}_2^{16}\text{O}$  321 GHz line (top left panel), the para- $\text{H}_2^{18}\text{O}$  322 GHz line (top right panel), and HDO 335 GHz line (bottom panel). The filter response is normalized by its standard deviation,  $\sigma$  (see also Loomis et al. 2018). We confirm the non-detection of all three lines as also found in the image-plane analyses.

## 4. Dust Continuum Image and Radial Profiles

Figure 7 shows the dust continuum emission map of the disk around HD 163296 at ALMA Band 7. The positions of bright

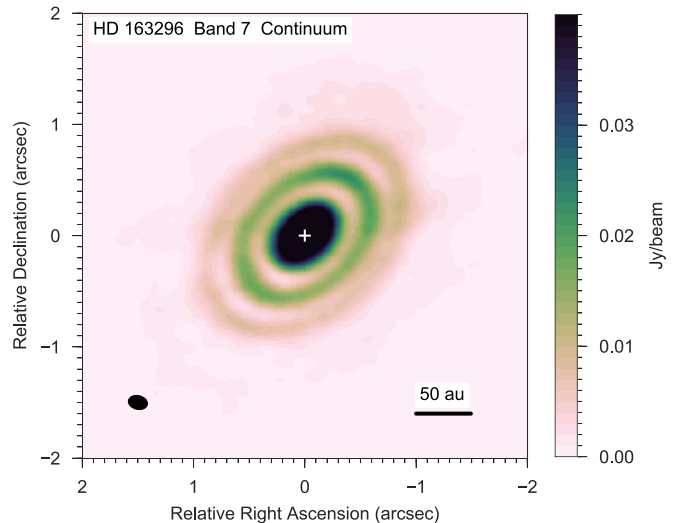


**Figure 7.** ALMA continuum image of the disk around HD 163296 at 0.9 mm (Band 7). The black ellipse in the bottom left corner shows the synthesized beam ( $0.174 \times 0.124$  arcsec). The black solid line in the bottom right corner shows the linear scale of 50 au in this disk.

rings and dark gaps in our observed Band 7 data are consistent with those indicated by the previous Cycle 2 observation of the Band 6 dust continuum emission (Isella et al. 2016). The resolution of the Band 7 image is  $\sim 1.4$  times smaller than that of Band 6 image reported in Isella et al. (2016), and  $\sim 2.4$  times smaller than that of our Band 6 image. In addition, Dent et al. (2019) recently reported the Band 7 dust continuum image of

<sup>19</sup> Freely available at <https://github.com/AstroChem/VISIBLE>.

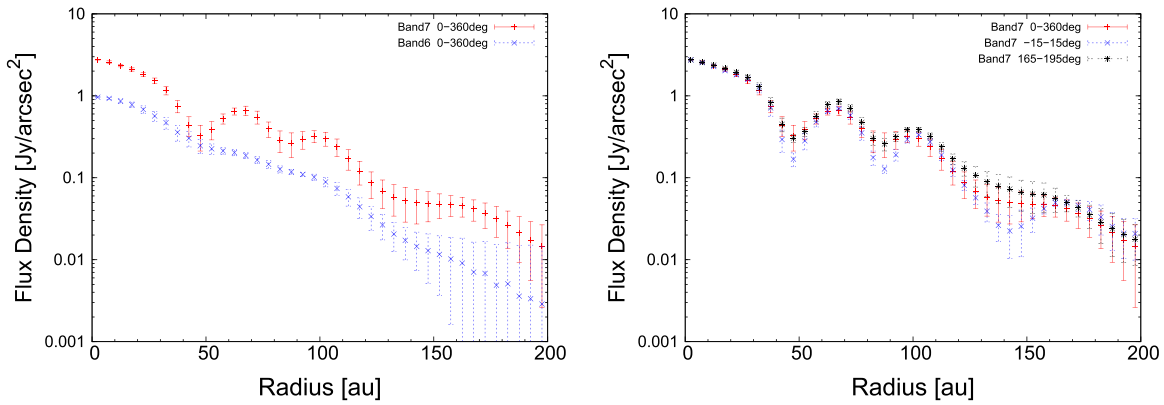


**Figure 8.** (Left panel): radial profiles of the flux densities in  $\text{Jy arcsec}^{-2}$  averaged over full azimuthal angle (0–360 deg) for Band 7 (red cross points) and Band 6 (blue cross points). (Right panel): Band 7 radial profiles of the flux densities in  $\text{Jy arcsec}^{-2}$  averaged over 0–360 deg (red cross points),  $-15 \sim 15$  deg (blue cross points), and  $-165 \sim 195$  deg (black asterisk points). The error bar is determined from the standard deviation through the azimuthal averaging. We determine the 0 deg as the southeast direction of the major axis.

**Table 3**

Calculated Peak Flux Densities and Total Fluxes of Our Target Water Lines in ALMA Band 7 with Different Outer Edges for the High Water Vapor Abundance Region

Isotope	Frequency (GHz)	Peak Flux Density (mJy) <sup>a,b</sup>					Total Flux ( $\text{W m}^{-2}$ ) <sup>a,b</sup>				
		5 au	8 au	11 au	14 au	20 au	5 au	8 au	11 au	14 au	20 au
ortho- $\text{H}_2^{16}\text{O}$	321.22568	5.9	8.9	9.1	9.2	9.2	$2.0 \times 10^{-21}$	$2.4 \times 10^{-21}$	$2.6 \times 10^{-21}$	$2.6 \times 10^{-21}$	$2.6 \times 10^{-21}$
para- $\text{H}_2^{18}\text{O}$	322.46517	3.0	5.7	8.7	10.9	14.4	$1.1 \times 10^{-21}$	$1.8 \times 10^{-21}$	$2.5 \times 10^{-21}$	$3.0 \times 10^{-21}$	$3.7 \times 10^{-21}$

**Notes.**

<sup>a</sup> When we calculate these model line fluxes, we include both dust and gas emission components, and we subtract dust emission components after the calculation. We investigate the values of dust opacity  $\kappa$  two times larger than that of our original Herbig Ae model (see also Figure 2 and Table 2). We set five values of the outer edge of high water vapor abundance region in the inner disk (5 au; original values: 5, 8, 11, 14, and 20 au where 8 au is the original value).

<sup>b</sup> In calculating these model line fluxes, we integrate the flux components within 20 au (circular aperture) from the central star.

this object, and the positions of rings and gaps in dust continuum emissions are consistent in both data.

To confirm the multiple ring and gap structures in detail, we plot the azimuthally averaged radial profiles of the dust continuum emission in Figure 8. There are three prominent gaps at around 50, 83 and 137 au, as previously reported in recent observations (Isella et al. 2016, 2018; Andrews et al. 2018; Dent et al. 2019). The gap depths in Band 7 data appear deeper than those in our Band 6 data because of the difference in spatial resolutions.

These multiple gaps and rings have also been found for several protoplanetary disks, such as HL Tau (e.g., ALMA Partnership et al. 2015; Akiyama et al. 2016; Carrasco-González et al. 2016; Pinte et al. 2016) and TW Hya (e.g., Akiyama et al. 2015; Rapson et al. 2015; Andrews et al. 2016; Nomura et al. 2016; Tsukagoshi et al. 2016; van Boekel et al. 2017; Huang et al. 2018a). Recently published observations from the DSHARP show that the continuum substructures are ubiquitous in disks. The most common substructures are narrow emission rings and depleted gaps, although large-scale spiral patterns and small arc-shaped azimuthal asymmetries are also present in some cases (e.g., Andrews et al. 2018; Huang et al. 2018b, 2018c; Isella et al. 2018).

The origins of multiple gap and ring patterns are still debated. Several theoretical studies proposed that the planet–disk interaction causes material clearance around the orbits of the planets (e.g., Kanagawa et al. 2015a, 2015b, 2016, 2018; Jin et al. 2016; Dong et al. 2018). There are other scenarios to

explain these patterns without planets, such as efficient particle growth and fragmentation of dust grains around snowlines (e.g., Ros & Johansen 2013; Banzatti et al. 2015; Zhang et al. 2015; Okuzumi et al. 2016; Pinilla et al. 2017), particle trapping at the pressure bump structures in the disk surface density close to the outer edge of the dead-zone (e.g., Flock et al. 2015; Pinilla et al. 2016; Ruge et al. 2016), zonal flows from magnetorotational instability (e.g., Béthune et al. 2016), secular gravitational instability (e.g., Takahashi & Inutsuka 2014, 2016; Tominaga et al. 2018), or baroclinic instability triggered by dust settling (Lorén-Aguilar & Bate 2015).

Current and future theoretical studies and observations of the dust continuum emission and gas emission (e.g., CO lines) at higher angular resolution with longer observation time are required to clarify the origins of these structures (e.g., van der Marel et al. 2018). Here, we note that recently van der Marel et al. (2019) suggested that such gap radii generally do not correspond to the orbital radii of snowlines of common molecules, such as CO,  $\text{CO}_2$ ,  $\text{CH}_4$ ,  $\text{N}_2$ , and  $\text{NH}_3$ , and the planet scenario can possibly explain the gaps, especially if the disk viscosity is low and the gaps can be explained by Neptune-mass planets.

## 5. Conclusions

In this paper, we used ALMA to obtain upper limit fluxes of submillimeter ortho- $\text{H}_2^{16}\text{O}$  321 GHz, para- $\text{H}_2^{18}\text{O}$  322 GHz, and HDO 335 GHz lines from the protoplanetary disk around the Herbig Ae star, HD 163296. The targeted lines are

considered to be the prime candidate water lines at submillimeter wavelengths to locate the position of the H<sub>2</sub>O snowline. These lines have not been detected, and we obtained the upper limit values of peak flux densities and total fluxes. We compared the upper limit fluxes with the values calculated by our model water line calculations with dust emission (Notsu et al. 2015, 2016, 2017, 2018). We constrained the line-emitting region and the dust opacity from the observations. We find that the millimeter dust opacity  $\kappa_{\text{mm}}$  must be larger than  $2.0 \text{ cm}^2 \text{ g}^{-1}$  to explain the water line properties, if the outer edge of the water vapor abundant region and also the position of the water snowline is beyond 8 au. In addition, the position of the water snowline will be inside 20 au, if the millimeter dust opacity  $\kappa_{\text{mm}}$  is  $2.0 \text{ cm}^2 \text{ g}^{-1}$ . We also report multiple ring and gap patterns in 0.9 mm (Band 7) dust continuum emission with 15 au resolution. The positions of bright rings and dust-depleted dark gaps are consistent with those indicated by the previous observations (Isella et al. 2016; Dent et al. 2019). Future observations of the dust continuum emission at higher angular resolution and submillimeter water lines with longer observation time are required to clarify the detailed structures and the position of the H<sub>2</sub>O snowline in the disk midplane.

We are grateful to Professor Inga Kamp and Dr. Satoshi Okuzumi for their useful comments. We thank the referee for many important suggestions and comments. This paper makes use of the following ALMA data: ADS/JAO.ALMA #2015.1.01259.S and ADS/JAO.ALMA #2013.1.00601.S. ALMA is a partnership of European Southern Observatory (ESO) (representing its member states), National Science Foundation (USA), and National Institutes of Natural Sciences (Japan), together with National Research Council (Canada), National Science Council and Academia Sinica Institute of Astronomy and Astrophysics (Taiwan), and Korea Astronomy and Space Science Institute (Korea), in cooperation with the Republic of Chile. The Joint ALMA Observatory is operated by ESO, Associated Universities, Inc/National Radio Astronomy Observatory (NRAO), and National Astronomical Observatory of Japan. Our numerical studies were carried out on SR16000 at Yukawa Institute for Theoretical Physics (YITP) and computer systems at Kwasan and Hida Observatory (KIPS) in Kyoto University, and PC cluster at Center for Computational Astrophysics, National Astronomical Observatory of Japan. ALMA Data analysis was carried out on the Multi-wavelength Data Analysis System operated by the Astronomy Data Center (ADC), National Astronomical Observatory of Japan. S.N. was supported by the ALMA Japan Research Grant of NAOJ Chile Observatory, NAOJ-ALMA-211. This work is supported by JSPS (Japan Society for the Promotion of Science) Grants-in-Aid for Scientific Research (KAKENHI) (grants No. 25108004, 25108005, 25400229, 15H03646, 15K17750, 17K05399, and 17K14244), by Grants-in-Aid for JSPS fellows (grant No. 16J06887), and by the Astrobiology Center Program of National Institutes of Natural Sciences (NINS; grant No. AB281013). C.W. acknowledges support from the Science and Technology Facilities Council (STFC; grant No. ST/R000549/1) and start-up funds from the University of Leeds. Astrophysics at Queen's University Belfast is supported by a grant from the STFC (ST/P000312/1). T.J.M. thanks Leiden Observatory for hospitality.

## ORCID iDs

Shota Notsu  <https://orcid.org/0000-0003-2493-912X>  
 Eiji Akiyama  <https://orcid.org/0000-0002-5082-8880>  
 Hideko Nomura  <https://orcid.org/0000-0002-7058-7682>  
 Catherine Walsh  <https://orcid.org/0000-0001-6078-786X>  
 Tomoya Hirota  <https://orcid.org/0000-0003-1659-095X>  
 Mitsuhiko Honda  <https://orcid.org/0000-0002-6172-9124>  
 Takashi Tsukagoshi  <https://orcid.org/0000-0002-6034-2892>  
 T. J. Millar  <https://orcid.org/0000-0001-5178-3656>

## References

- Aikawa, Y., & Nomura, H. 2006, *ApJ*, **642**, 1152  
 Akiyama, E., Hasegawa, Y., Hayashi, M., & Iguchi, S. 2016, *ApJ*, **818**, 158  
 Akiyama, E., Momose, M., Hayashi, H., & Kitamura, Y. 2011, *PASJ*, **63**, 1059  
 Akiyama, E., Muto, T., Kusakabe, N., et al. 2015, *ApJL*, **802**, L17  
 ALMA Partnership, Brogan, C. L., Pérez, L. M., et al. 2015, *ApJL*, **808**, L3  
 Andrews, S. M., Huang, J., Pérez, L. M., et al. 2018, *ApJL*, **869**, L41  
 Andrews, S. M., Wilner, D. J., Zhu, Z., et al. 2016, *ApJL*, **820**, L40  
 Antonellini, S., Bremer, J., Kamp, I., et al. 2017, *A&A*, **597**, A72  
 Antonellini, S., Kamp, I., Lahuis, F., et al. 2016, *A&A*, **585**, A61  
 Antonellini, S., Kamp, I., Riviere-Marichalar, P., et al. 2015, *A&A*, **582**, A105  
 Banzatti, A., Pinilla, P., Ricci, L., et al. 2015, *ApJL*, **815**, L15  
 Banzatti, A., Pontoppidan, K. M., Salyk, C., et al. 2017, *ApJ*, **834**, 152  
 Béthune, W., Lesur, G., & Ferreira, J. 2016, *A&A*, **589**, A87  
 Blevins, S. M., Pontoppidan, K. M., Banzatti, A., et al. 2016, *ApJ*, **818**, 22  
 Boneberg, D. M., Panić, O., Haworth, T. J., Clarke, C. J., & Min, M. 2016, *MNRAS*, **461**, 385  
 Booth, A. S., Walsh, C., Kama, M., et al. 2018, *A&A*, **611**, A16  
 Bosman, A. D., Walsh, C., & van Dishoeck, E. F. 2018, *A&A*, **618**, A182  
 Carney, M. T., Fedele, D., Hogerheijde, M. R., et al. 2018, *A&A*, **614**, A106  
 Carney, M. T., Hogerheijde, M. R., Guzmán, V. V., et al. 2019, *A&A*, **623**, 124  
 Carney, M. T., Hogerheijde, M. R., Loomis, R. A., et al. 2017, *A&A*, **605**, A21  
 Carr, J. S., & Najita, J. R. 2008, *Sci*, **319**, 1504  
 Carr, J. S., Najita, J. R., & Salyk, C. 2018, *RNAAS*, **2**, 169  
 Carrasco-González, C., Henning, T., Chandler, C. J., et al. 2016, *ApJL*, **821**, L16  
 Cieza, L. A., Casassus, S., Tobin, J., et al. 2016, *Natur*, **535**, 258  
 Dent, W. R. F., Greaves, J. S., & Coulson, I. M. 2005, *MNRAS*, **359**, 663  
 Dent, W. R. F., Pinte, C., Cortes, P. C., et al. 2019, *MNRAS*, **482**, L29  
 Dong, R., Li, S., Chiang, E., & Li, H. 2018, *ApJ*, **866**, 110  
 Draine, B. T. 2006, *ApJ*, **636**, 1114  
 Du, F., Bergin, E. A., Hogerheijde, M., et al. 2017, *ApJ*, **842**, 98  
 Favre, C., Cleeves, L. I., Bergin, E. A., Qi, C., & Blake, G. A. 2013, *ApJL*, **776**, L38  
 Fedele, D., Bruderer, S., van Dishoeck, E. F., et al. 2012, *A&A*, **544**, LL9  
 Fedele, D., Bruderer, S., van Dishoeck, E. F., et al. 2013, *A&A*, **559**, AA77  
 Flock, M., Ruge, J. P., Dzyurkevich, N., et al. 2015, *A&A*, **574**, A68  
 Gaia Collaboration, Brown, A. G. A., Vallenari, A., et al. 2018, *A&A*, **616**, A1  
 Guidi, G., Ruane, G., Williams, J. P., et al. 2018, *MNRAS*, **479**, 1505  
 Guidi, G., Tazzari, M., Testi, L., et al. 2016, *A&A*, **588**, A112  
 Hama, T., Kouchi, A., & Watanabe, N. 2016, *Sci*, **351**, 65  
 Hama, T., Kouchi, A., & Watanabe, N. 2018, *ApJL*, **857**, L13  
 Hama, T., & Watanabe, N. 2013, *ChRv*, **113**, 8783  
 Harsono, D., Bruderer, S., & van Dishoeck, E. F. 2015, *A&A*, **582**, A41  
 Hayashi, C. 1981, *PThPS*, **70**, 35  
 Hayashi, C., Nakazawa, K., & Nakagawa, Y. 1985, in *Protostars and Planets II*, ed. D. C. Black & M. S. Matthews (Tucson, AZ: Univ. Arizona Press), 1100  
 Hogerheijde, M. R., Bergin, E. A., Brinch, C., et al. 2011, *Sci*, **334**, 338  
 Hogerheijde, M. R., & van der Tak, F. F. S. 2000, *A&A*, **362**, 697  
 Honda, M., Inoue, A. K., Fukagawa, M., et al. 2009, *ApJL*, **690**, L110  
 Honda, M., Kudo, T., Takatsuki, S., et al. 2016, *ApJ*, **821**, 2  
 Honda, M., Maaskant, K., Okamoto, Y. K., et al. 2015, *ApJ*, **804**, 143  
 Huang, J., Andrews, S. M., Cleeves, L. I., et al. 2018a, *ApJ*, **852**, 122  
 Huang, J., Andrews, S. M., Dullemond, C. P., et al. 2018b, *ApJL*, **869**, L42  
 Huang, J., Andrews, S. M., Pérez, L. M., et al. 2018c, *ApJL*, **869**, L43  
 Ida, S., & Guillot, T. 2016, *A&A*, **596**, L3  
 Isella, A., Guidi, G., Testi, L., et al. 2016, *PhRvL*, **117**, 251101  
 Isella, A., Huang, J., Andrews, S. M., et al. 2018, *ApJL*, **869**, L49  
 Jin, S., Li, S., Isella, A., Li, H., & Ji, J. 2016, *ApJ*, **818**, 76  
 Jørgensen, J. K., & van Dishoeck, E. F. 2010, *ApJL*, **710**, L72  
 Kamp, I., Thi, W.-F., Meeus, G., et al. 2013, *A&A*, **559**, A24  
 Kanagawa, K. D., Muto, T., Tanaka, H., et al. 2015a, *ApJL*, **806**, L15

- Kanagawa, K. D., Muto, T., Tanaka, H., et al. 2016, *PASJ*, 68, 43
- Kanagawa, K. D., Tanaka, H., Muto, T., Tanigawa, T., & Takeuchi, T. 2015b, *MNRAS*, 448, 994
- Kanagawa, K. D., Tanaka, H., & Szuszkiewicz, E. 2018, *ApJ*, 861, 140
- Liu, S.-F., Jin, S., Li, S., Isella, A., & Li, H. 2018, *ApJ*, 857, 87
- Loomis, R. A., Öberg, K. I., Andrews, S. M., et al. 2018, *AJ*, 155, 182
- Lorén-Aguilar, P., & Bate, M. R. 2015, *MNRAS*, 453, L78
- Malfait, K., Waelkens, C., Bouwman, J., de Koter, A., & Waters, L. B. F. M. 1999, *A&A*, 345, 181
- Mandell, A. M., Bast, J., van Dishoeck, E. F., et al. 2012, *ApJ*, 747, 92
- Mathews, G. S., Klaassen, P. D., Juhász, A., et al. 2013, *A&A*, 557, A132
- McClure, M. K., Espaillat, C., Calvet, N., et al. 2015, *ApJ*, 799, 162
- McClure, M. K., Manoj, P., Calvet, N., et al. 2012, *ApJL*, 759, L10
- Meeus, G., Montesinos, B., Mendigutía, I., et al. 2012, *A&A*, 544, AA78
- Min, M., Bouwman, J., Dominik, C., et al. 2016, *A&A*, 593, A11
- Miyake, K., & Nakagawa, Y. 1993, *Icar*, 106, 20
- Monnier, J. D., Harries, T. J., Aarnio, A., et al. 2017, *ApJ*, 838, 20
- Morbidelli, A., Bitsch, B., Crida, A., et al. 2016, *Icar*, 267, 368
- Morbidelli, A., Chambers, J., Lunine, J. I., et al. 2000, *M&PS*, 35, 1309
- Morbidelli, A., Lunine, J. I., O'Brien, D. P., Raymond, S. N., & Walsh, K. J. 2012, *AREPS*, 40, 251
- Mumma, M. J., Weaver, H. A., & Larson, H. P. 1987, *A&A*, 187, 419
- Nomura, H., Aikawa, Y., Tsujimoto, M., Nakagawa, Y., & Millar, T. J. 2007, *ApJ*, 661, 334
- Nomura, H., & Millar, T. J. 2005, *A&A*, 438, 923
- Nomura, H., Tsukagoshi, T., Kawabe, R., et al. 2016, *ApJL*, 819, L7
- Notsu, S., Nomura, H., Ishimoto, D., et al. 2015, in *ASP Conf. Ser.* 499, *Revolution in Astronomy with ALMA: The Third Year*, ed. D. Iono et al. (San Francisco, CA: ASP), 289
- Notsu, S., Nomura, H., Ishimoto, D., et al. 2016, *ApJ*, 827, 113
- Notsu, S., Nomura, H., Ishimoto, D., et al. 2017, *ApJ*, 836, 118
- Notsu, S., Nomura, H., Walsh, C., et al. 2018, *ApJ*, 855, 62
- Öberg, K. I., Murray-Clay, R., & Bergin, E. A. 2011, *ApJL*, 743, L16
- Oka, A., Nakamoto, T., & Ida, S. 2011, *ApJ*, 738, 141
- Okuzumi, S., Momose, M., Sirono, S.-i., Kobayashi, H., & Tanaka, H. 2016, *ApJ*, 821, 82
- Okuzumi, S., Tanaka, H., Kobayashi, H., & Wada, K. 2012, *ApJ*, 752, 106
- Perryman, M. A. C., Lindegren, L., Kovalevsky, J., et al. 1997, *A&A*, 323, L49
- Persson, M. V., Jørgensen, J. K., & van Dishoeck, E. F. 2012, *A&A*, 541, A39
- Pinilla, P., Benisty, M., Birnstiel, T., et al. 2014, *A&A*, 564, A51
- Pinilla, P., Flock, M., Ovelar, M. d. J., & Birnstiel, T. 2016, *A&A*, 596, A81
- Pinilla, P., Pohl, A., Stammer, S. M., & Birnstiel, T. 2017, *ApJ*, 845, 68
- Pinte, C., Dent, W. R. F., Ménard, F., et al. 2016, *ApJ*, 816, 25
- Pinte, C., Price, D. J., Ménard, F., et al. 2018, *ApJL*, 860, L13
- Piso, A.-M. A., Öberg, K. I., Birnstiel, T., & Murray-Clay, R. A. 2015, *ApJ*, 815, 109
- Piso, A.-M. A., Pegues, J., & Öberg, K. I. 2016, *ApJ*, 833, 203
- Podio, L., Kamp, I., Codella, C., et al. 2013, *ApJL*, 766, L5
- Pontoppidan, K. M., Salyk, C., Blake, G. A., et al. 2010a, *ApJ*, 720, 887
- Pontoppidan, K. M., Salyk, C., Blake, G. A., & Käufel, H. U. 2010b, *ApJL*, 722, L173
- Qi, C., D'Alessio, P., Öberg, K. I., et al. 2011, *ApJ*, 740, 84
- Qi, C., Öberg, K. I., Andrews, S. M., et al. 2015, *ApJ*, 813, 128
- Rapson, V. A., Kastner, J. H., Millar-Blanchaer, M. A., & Dong, R. 2015, *ApJL*, 815, L26
- Raymond, S. N., & Izidoro, A. 2017, *Icar*, 297, 134
- Reboussin, L., Wakelam, V., Guilloteau, S., Hersant, F., & Dutrey, A. 2015, *A&A*, 579, A82
- Riviere-Marichalar, P., Ménard, F., Thi, W. F., et al. 2012, *A&A*, 538, L3
- Ros, K., & Johansen, A. 2013, *A&A*, 552, A137
- Rothman, L. S., Gordon, I. E., Babikov, Y., et al. 2013, *JQSRT*, 130, 4
- Ruge, J. P., Flock, M., Wolf, S., et al. 2016, *A&A*, 590, A17
- Rybicki, G. B., & Lightman, A. P. (ed.) 1986, *Radiative Processes in Astrophysics* (New York: Wiley-VCH)
- Salinas, V. N., Hogerheijde, M. R., Mathews, G. S., et al. 2017, *A&A*, 606, A125
- Salinas, V. N., Hogerheijde, M. R., Murillo, N. M., et al. 2018, *A&A*, 616, A45
- Salyk, C., Lacy, J., Richter, M., et al. 2019, *ApJ*, 874, 24
- Salyk, C., Pontoppidan, K. M., Blake, G. A., et al. 2008, *ApJL*, 676, L49
- Salyk, C., Pontoppidan, K. M., Blake, G. A., Najita, J. R., & Carr, J. S. 2011, *ApJ*, 731, 130
- Sato, T., Okuzumi, S., & Ida, S. 2016, *A&A*, 589, A15
- Schöier, F. L., van der Tak, F. F. S., van Dishoeck, E. F., & Black, J. H. 2005, *A&A*, 432, 369
- Schoonenberg, D., Okuzumi, S., & Ormel, C. W. 2017, *A&A*, 605, L28
- Schwarz, K. R., Bergin, E. A., Cleeves, L. I., et al. 2016, *ApJ*, 823, 91
- Schwarz, K. R., Bergin, E. A., Cleeves, L. I., et al. 2018, *ApJ*, 856, 85
- Takahashi, S. Z., & Inutsuka, S.-i. 2014, *ApJ*, 794, 55
- Takahashi, S. Z., & Inutsuka, S.-i. 2016, *AJ*, 152, 184
- Teague, R., Bae, J., Bergin, E. A., Birnstiel, T., & Foreman-Mackey, D. 2018, *ApJL*, 860, L12
- Terada, H., & Tokunaga, A. T. 2017, *ApJ*, 834, 115
- Terada, H., Tokunaga, A. T., Kobayashi, N., et al. 2007, *ApJ*, 667, 303
- Tominaga, R. T., Inutsuka, S.-i., & Takahashi, S. Z. 2018, *PASJ*, 70, 3
- Tsukagoshi, T., Nomura, H., Muto, T., et al. 2016, *ApJL*, 829, L35
- van Boekel, R., Henning, T., Menu, J., et al. 2017, *ApJ*, 837, 132
- van den Ancker, M. E., The, P. S., Tjin A Djie, H. R. E., et al. 1997, *A&A*, 324, L33
- van der Marel, N., Dong, R., di Francesco, J., et al. 2019, *ApJ*, 872, 112
- van der Marel, N., Williams, J. P., & Bruderer, S. 2018, *ApJL*, 867, L14
- van Dishoeck, E. F., Bergin, E. A., Lis, D. C., & Lunine, J. I. 2014, in *Protostars and Planets VI*, ed. H. Beuther et al. (Tucson, AZ: Univ. Arizona Press), 835
- van't Hoff, M. L. R., Tobin, J. J., Trapman, L., et al. 2018, *ApJL*, 864, L23
- Walsh, C., Millar, T. J., & Nomura, H. 2010, *ApJ*, 722, 1607
- Walsh, C., Nomura, H., Millar, T. J., & Aikawa, Y. 2012, *ApJ*, 747, 114
- Walsh, C., Nomura, H., & van Dishoeck, E. 2015, *A&A*, 582, A88
- Walsh, K. J., Morbidelli, A., Raymond, S. N., O'Brien, D. P., & Mandell, A. M. 2011, *Natur*, 475, 206
- Wilson, T. L., & Rood, R. 1994, *ARA&A*, 32, 191
- Woodall, J., Agúndez, M., Markwick-Kemper, A. J., & Millar, T. J. 2007, *A&A*, 466, 1197
- Zhang, K., Bergin, E. A., Blake, G. A., et al. 2016, *ApJL*, 818, L16
- Zhang, K., Bergin, E. A., Blake, G. A., Cleeves, L. I., & Schwarz, K. R. 2017, *NatAs*, 1, 0130
- Zhang, K., Blake, G. A., & Bergin, E. A. 2015, *ApJL*, 806, L7
- Zhang, K., Pontoppidan, K. M., Salyk, C., & Blake, G. A. 2013, *ApJ*, 766, 82